Effect of crystal anisotropy on the infrared reflectivity of 6*H*-SiC

F. Engelbrecht and R. Helbig
Institute of Applied Physics, University of Erlangen-Nürnberg, Staudtstrasse 7, 91058 Erlangen, Germany
(Received 16 March 1993; revised manuscript received 11 August 1993)

Polarized infrared reflectivity spectra of 6*H*-SiC single crystals under different angles of incidence are reported. A new sharp line in the reststrahl band was observed in the extraordinary ray, whose line shape is dependent on the angle of incidence. It was possible to show that crystal anisotropy of 6*H*-SiC is the reason for the new line in the reflectivity spectrum. A numerical calculation using a Lorentz oscillator model confirmed this result. Two weak one-phonon absorption lines in the reststrahl-band region for $\mathbf{E}\|c$ were observed. Furthermore, we found a line at 859 cm^{-1} in the extraordinary ray and an unusual structure near ω_{TO} in the reststrahl band of parallel *c*-cut 6*H*-SiC samples, which could not be explained in terms of the classical Lorentz oscillator model.

I. INTRODUCTION

Infrared reflectivity spectra in SiC were reported previously by several authors.[1–13] As shown in Ref. 14 it is possible to identify the polytype of a silicon carbide crystal through the fine structure in the reststrahl band. This report deals with polarized infrared reflectivity spectra of 6*H*-SiC single crystals under different angles of incidence. In addition to results already published on the infrared reflectivity of SiC polytypes we found new lines and structures in the reststrahl band of 6*H*-SiC which we will describe in this paper.

A. Crystallographic structure of 6*H*-SiC

Figure 1 shows the unit cell of 6*H*-SiC. The stacking order of the *C-Si* layers is *A-B-C-A-C-B*. This arrangement of the atoms leads to a hexagonal structure with a sixfold symmetry axis along the stacking direction (*c* axis). The crystal anisotropy of 6*H*-SiC is introduced into this material by this hexagonal structure. The complex crystallographic structure of 6*H*-SiC (six silicon and carbon atoms per unit cell each) is the reason for the large number of infrared active phonons (ten IR active branches) in this material. Thus this polytype shows some polarization-dependent absorption lines in the reststrahl band, which make it ideal for studying the influence of (a weak) crystal anisotropy on the infrared reflectivity.

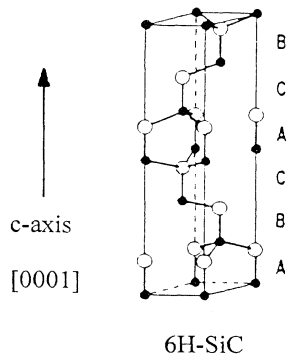

FIG. 1. Unit cell of 6*H*-SiC (hexagonal symmetry).

B. Classical Lorentz oscillator dispersion theory

The classical Lorentz oscillator model dispersion formula for v TO phonons ω_j,[15]

$$\epsilon(\omega)=\epsilon_\infty+\sum_{j=1}^{v}\frac{4\pi\rho_j\omega_j^2}{\omega_j^2-\omega^2-i\Gamma_j\omega}\ , \tag{1}$$

in the region of the reststrahlen frequencies can be obtained by using the fundamental equations of lattice dynamics combined with Maxwell's equations (cf. Refs. 16–19). In Eq. (1) ϵ_∞ is the high-frequency dielectric constant, ω_j the frequency, ρ_j the oscillator strength, and Γ_j the damping constant of the jth TO phonon. Taking the anharmonic phonon-phonon interaction into account through a quantum-mechanical treatment, Γ is a frequency- and temperature-dependent function $\Gamma=\Gamma(\omega,T)$.[20] However, these parameters depend on each other due to the generalized (including damping) Lyddane-Sachs-Teller (GLST) relation which has the following form in the case of a single resonance:[21]

$$\frac{\epsilon_0}{\epsilon_\infty}=\frac{\omega_{LO}^2+\Gamma^2/4}{\omega_{TO}^2+\Gamma^2/4}\ . \tag{2}$$

For $\Gamma=0$ this formula reduces to the well-known Lyddane-Sachs-Teller relation.[22]

C. Dispersion relation of phononic polariton

In Eq. (1) only polarization by the electrical field **E** was taken into account. A rigorous treatment also requires consideration of the coupling with the **B** field according to the Maxwell equation $\nabla\times\mathbf{E}=-(1/c)\partial\mathbf{B}/\partial t$. A more precise description of the photon-phonon interaction, which is consistent with Maxwell's equations, is the so-called polariton concept developed by Born and Huang.[16]

In an anisotropic, nonmagnetic medium without electrical currents, the wave equation is given by[23,24]

$$\left| \frac{\omega^2}{c^2}\epsilon_{ij}(\omega,\mathbf{k}) - k^2\delta_{ij} + k_i k_j \right| = 0 \ . \tag{3}$$

Herein ϵ_{ij} denotes the ijth component of the dielectric tensor and k_i the ith component of the wave vector.

Solutions of this equation for $\omega(\mathbf{k})$, especially for uniaxial crystals, have been detailed discussed in the literature.[25–27]

D. Spatial dispersion

Spatial dispersion means the nonlocal behavior of the dielectric function ϵ, which depends not only on ω but also on the wave vector $\mathbf{k}$:

$$\epsilon = \epsilon(\omega,\mathbf{k}) \ . \tag{4}$$

This results in new phenomena, which have been demonstrated in the reflectivity spectra of excitonic polaritons in direct semiconductors with a uniaxial lattice.[28,29] In principle such a dependence on $\mathbf{k}$ also is possible in the infrared spectral range. The resonant TO phonon has a wave-vector dependence $\omega_{\mathrm{TO,phonon}} = \omega(\mathbf{k})$ as a consequence of the phonon dispersion relations. The wave vector in the crystal $\mathbf{k}'$ is connected with the vacuum wave vector k by $k' = nk$, where n denotes the refractive index in the material. For instance assuming a maximum value of $n \approx 20$ (depending on damping) at the resonance frequency ω_{TO} of the strongest phonon one can estimate an upper limit of k' to be less than 2×10^{-3} times the extension of the Brillouin zone π/a in the infrared region. So one expects only a very slight dependence of ϵ on the absolute value of the wave vector $\mathbf{k}$. Thus, in uniaxial crystals ϵ describing the phononic polariton depends only on the direction of $\mathbf{k}$. This is called directional dispersion and will be discussed in the next section.

II. INFLUENCE OF CRYSTAL ANISOTROPY ON INFRARED REFLECTIVITY IN UNIAXIAL CRYSTALS

The influence of crystal anisotropy on infrared reflectivity was discussed theoretically by Lang and Pashabekova,[30] but no experimental results have been available to test this theory to date. Their point of view is somewhat different from the experimental situation in our experiments. They discussed infrared reflectivity of crystals in the case of normal incident radiation on a surface cut with an angle θ to the optical axis of the crystal. In contrast to that, the measurements in this work were performed on crystals cut parallel or perpendicular to the c axis. However, a similar situation, which provides comparable results, was achieved by using different angles of incidence.

In uniaxial media two different solutions of the wave equation exist, which describe the ordinary and the extraordinary rays: The ordinary ray is polarized perpendicular to the plane defined by the c axis and the wave vector $\mathbf{k}$; the extraordinary ray is polarized in the plane defined by the c axis and the wave vector $\mathbf{k}$. If one neglects the coupling by the magnetic field $\mathbf{B}$ (this is assumed in Ref. 30), the ordinary ray is not affected by crystal anisotropy. The optical properties (here reflectivity) are independent of the angle between the c axis and direction of propagation. In the case of the extraordinary ray the electrical field $\mathbf{E}$ lies in the plane defined by the c axis and the wave vector and crystal anisotropy causes directional dispersion: Here the energies of the lattice modes depend on the propagation direction in the crystal, and the pure transverse or longitudinal character and symmetry of the optical phonons disappears due to mixing effects, except for $\theta = 0°$ and $\theta = 90°$. Directional dispersion and its calculation in uniaxial crystals has been examined in Refs. 32–34. As described there, it is possible to calculate the explicit form of the functions $\epsilon_\infty(\theta)$, $\rho_i(\theta)$, $\omega_i(\theta)$, and $\Gamma_i(\theta)$ for arbitrary angles θ if all the parameters in Eq. (5) are known

$$\begin{aligned}
\epsilon_\perp(\omega) &= \epsilon_\perp^\infty + \sum_{j=1}^{v} \frac{4\pi\rho_{\perp,j}\omega_{\perp,j}^2}{\omega_{\perp,j}^2 - \omega^2 - i\Gamma_{\perp,j}\omega} \ , \\
\epsilon_\parallel(\omega) &= \epsilon_\parallel^\infty + \sum_{k=1}^{w} \frac{4\pi\rho_{\parallel,k}\omega_{\parallel,k}^2}{\omega_{\parallel,k}^2 - \omega^2 - i\Gamma_{\parallel,k}\omega}
\end{aligned} \tag{5}$$

(v and w are the number of active TO phonons according to selection rules for $\mathbf{E}\perp c$ and $\mathbf{E}\parallel c$). The degree of mixing depends on the influence of the crystal anisotropy compared with the magnitude of the local field built up from the lattice modes (longitudinal-transverse split). In the case of 6H-SiC, 4H-SiC, and ZnO, which all have hexagonal symmetry C_{6v}, for example, the effect of crystal anisotropy is weaker than the longitudinal-transverse split.[25]

For calculating the reflectivity of a uniaxial crystal, the Fresnel equation (3) must be solved with $\epsilon_{11} = \epsilon_{22} = \epsilon_\perp, \epsilon_{33} = \epsilon_\parallel$:

$$\begin{aligned}
&[\omega^2\epsilon_\perp(\omega) - c^2k^2]\{\epsilon_\perp(\omega)[\omega^2\epsilon_\parallel(\omega) - c^2k^2]s_\perp \\
&\qquad + \epsilon_\parallel(\omega)[\omega^2\epsilon_\perp(\omega) - c^2k^2]s_\parallel\} = 0 \ ;
\end{aligned} \tag{6}$$

here $\mathbf{k}$ is the wave vector and $\mathbf{s} = (s_\perp, s_\parallel)$ its direction with $s_\perp = (s_1^2 + s_2^2)^{1/2}$ and $s_\parallel = s_3$. The solutions of Eq. (6) correspond to the ordinary ray

$$\epsilon(\omega) = \epsilon_\perp(\omega) \tag{7}$$

and the extraordinary ray

$$\epsilon(\omega,\theta) = \frac{\epsilon_\perp(\omega)\epsilon_\parallel(\omega)}{\epsilon_\perp(\omega)\sin^2\theta + \epsilon_\parallel(\omega)\cos^2\theta} \ , \tag{8}$$

where the angle θ between the optical axis and the direction of propagation was introduced. Regarding a single TO phonon without damping ($\Gamma = 0$) and writing $\epsilon_\perp$ and $\epsilon_\parallel$ in the form

$$\epsilon(\omega) = \epsilon_\infty \frac{\omega_{\mathrm{LO}}^2 - \omega^2}{\omega_{\mathrm{TO}}^2 - \omega^2} \ ,$$

$\epsilon(\omega,\theta)$ is given by

$$\epsilon(\omega,\theta)=\frac{(\omega_{\mathrm{LO},\perp}^2-\omega^2)(\omega_{\mathrm{LO},\parallel}^2-\omega^2)}{(\omega_{\mathrm{LO},\perp}^2-\omega^2)(\omega_{\mathrm{TO},\parallel}^2-\omega^2)\sin^2(\theta)/\epsilon_{\infty,\parallel}+(\omega_{\mathrm{LO},\parallel}^2-\omega^2)(\omega_{\mathrm{TO},\perp}^2-\omega^2)\cos^2(\theta)/\epsilon_{\infty,\perp}}\ .$$

$\epsilon(\omega,\theta)$ has two propagation-direction-dependent poles $\omega_I(\theta)$ and $\omega_{II}(\theta)$ due to the roots of the denominator, and in the case of $\omega=\omega_{\mathrm{LO},\perp}$ or $\omega=\omega_{\mathrm{LO},\parallel}$ one obtains $\epsilon=0$. The direction dependence of the resonance frequencies $\omega_I(\theta)$ and $\omega_{II}(\theta)$ in 6*H*-SiC is shown in Fig. 2. Consequently two different reststrahl bands appear in the reflectivity spectrum of the extraordinary ray. In general their precise form depends on the angle θ between the direction of propagation and direction of the *c* axis on the one hand and the angle of radiation incidence ϕ on the other hand. The frequency range of the two reststrahl bands in 6*H*-SiC is shown in Fig. 2 (hatched area).

III. EXPERIMENTAL DETAILS

All reflectivity spectra described here were obtained on samples cut from 6*H*-SiC boules grown at the Siemens Research Laboratory in Erlangen with a modified Lely method proposed by Ziegler *et al.*[31] Some of the samples were prepared with the optical axis parallel to and others with the optical axis perpendicular to the polished surface. The samples were treated with hydrogen fluoride acid to ensure that no oxide layer covers the surface. They were cleaned with destillated water and acetone in an ultrasonic bath before measurement.

The samples were *n* type with nitrogen concentrations between 0.5 and 1.0×10^{17} cm^{-3} at room temperature. The identification of the polytype was performed by measuring low-temperature photoluminescence due to bound excitons at neutral nitrogen donor atoms.[35] All reflectivity spectra were recorded at room temperature using a Nicolet infrared Fourier spectrometer type FTIR 740 at a resolution of 1 cm^{-1}. The Spectra Tech specular reflectivity model 500 and a polarizer were used for measurements under different angles of incidence from 30° to 70°. In the experimental spectra only relative reflectivities are presented, due to the fact that absolute reflectivity is difficult to determine.

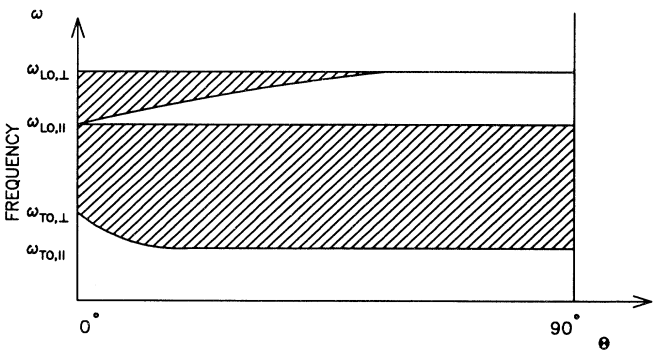

FIG. 2. Origin of two reststrahl bands in uniaxial crystals for the extraordinary ray demonstrated in the case of 6*H*-SiC (θ: angle between optical axis and propagation direction; hatched part: area of high reflectivity).

IV. ANGLE- AND POLARIZATION-DEPENDENT MEASUREMENTS OF 6*H*-SiC RESTSTRAHL BAND

Four experimental geometries were used for measurements: (1) geometry *G*1: ⊥ *c*-cut sample, **E**∥*c*; (2) geometry *G*2: ⊥ *c*-cut sample, **E**⊥*c*; (3) geometry *G*3: ∥ *c*-cut sample, **E**∥*c*; and, (4) geometry *G*4: ∥ *c*-cut sample, **E**⊥*c*. For each of these geometries, the reflectivity spectra were recorded with following angles of incidence: $\phi=30°$, 40°, 50°, 60°, 70°. Four main features appeared in the spectra: (a) a sharp line at the high-energy part of the reststrahl band ($\omega\approx\omega_{\mathrm{LO}}$) under flat angles of incidence in the extraordinary ray in crystal geometries *G*1 (⊥ *c* cut) and *G*3 (∥ *c* cut), (b) two peaks at 889 and 884 cm^{-1} in the middle of the reststrahl band in the extraordinary ray, (c) a line at 859 cm^{-1} in the middle of the reststrahl band in the extraordinary ray under 60° and 70° angles of incidence, and (d) a broad hump on the low-energy side ($\omega\approx800$ cm^{-1}) of the reststrahl band in geometries *G*3 and *G*4.

(a) A sharp line at the high-energy part of the reststrahl band is visible in the extraordinary ray in both crystal orientations (geometries *G*1 and *G*3) under flat angles of incidence (*G*1: $\phi\geq50°$; *G*3: $\phi\geq40°$), which increases as the angle of incidence becomes more flat. This line is a consequence of the anistropic of the 6*H*-SiC lattice as discussed in Sec. II. In this material (the case of low anisotropy compared with TO-LO splitting) crystal anisotropy can be observed in infrared reflectivity spectra by the shift of the reststrahl band (area of high reflectivity between ω_{TO} and ω_{LO}: **E**∥*c*: $\omega_{\mathrm{TO},\parallel}=788$ cm^{-1}, $\omega_{\mathrm{LO},\parallel}=964$ cm^{-1}; **E**⊥*c*: $\omega_{\mathrm{TO},\perp}=797$ cm^{-1}, $\omega_{\mathrm{LO},\perp}=970$ cm^{-1}) for the two polarization directions [cf. Figs. 3(c), and 3(d)], and, additionally, in the appearance of this spike line in the extraordinary ray [cf. Figs. 4(c), and 5(a)]. Our measurements are the first systematic description of this line. Only Collins *et al.*[36] report on a similar spike appearing in the extraordinary ray in AlN, but the line was erroneously regarded as a two-phonon transition.

(b) Other remarkable structures are the two peaks at 889 and 884 cm^{-1} in the middle of the reststrahl band for samples cut parallel to the *c* axis and polarization **E**∥*c* [geometry *G*3; cf. Figs. 3(c), 4(c), 5(c), 6(c), and 7(c)]. They also appeared in the *G*1 geometry, e.g., Fig. 5(a) for flat angles of incidence; however, their intensities in the *G*1 geometry were much weaker than in the *G*3 geometry. They can be identified with phonon lines found in Raman scattering measurements by Feldman *et al.*[37] due to the infrared and Raman selection rules for a hexagonal lattice (C_{6v} symmetry) (Ref. 38) of TO phonons having A_1 symmetry.

(c) Furthermore a very weak line at 859 cm^{-1} was observed in the reflectivity spectra. It first became visible in

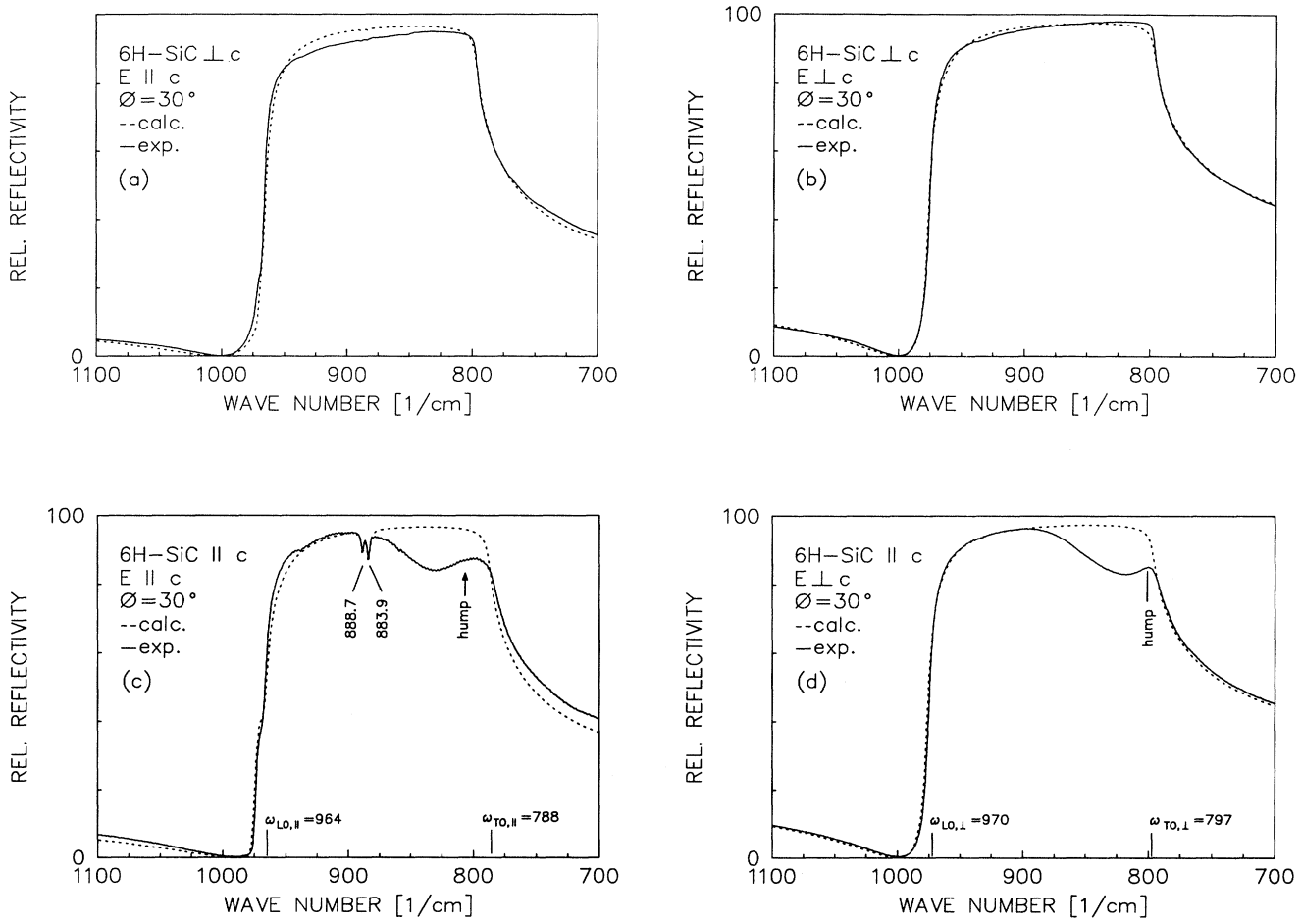

FIG. 3. (a) 6*H*-SiC reflectivity spectrum *G*1: ⊥ *c*-cut sample, $\mathbf{E}\|c,\phi=30°$; (b) 6*H*-SiC reflectivity spectrum *G*2: ⊥ *c*-cut sample, $\mathbf{E}\perp c,\phi=30°$; (c) 6*H*-SiC reflectivity spectrum *G*3: ∥*c*-cut sample, $\mathbf{E}\|c,\phi=30°$. Two weak phonon absorption lines appear in the middle of the reststrahl band; there is also a hump structure observable near ω_{TO} (d) 6*H*-SiC reflectivity spectrum *G*4: ∥ *c*-cut sample, $\mathbf{E}\perp c,\phi=30°$. The hump structure appears also in the ordinary ray.

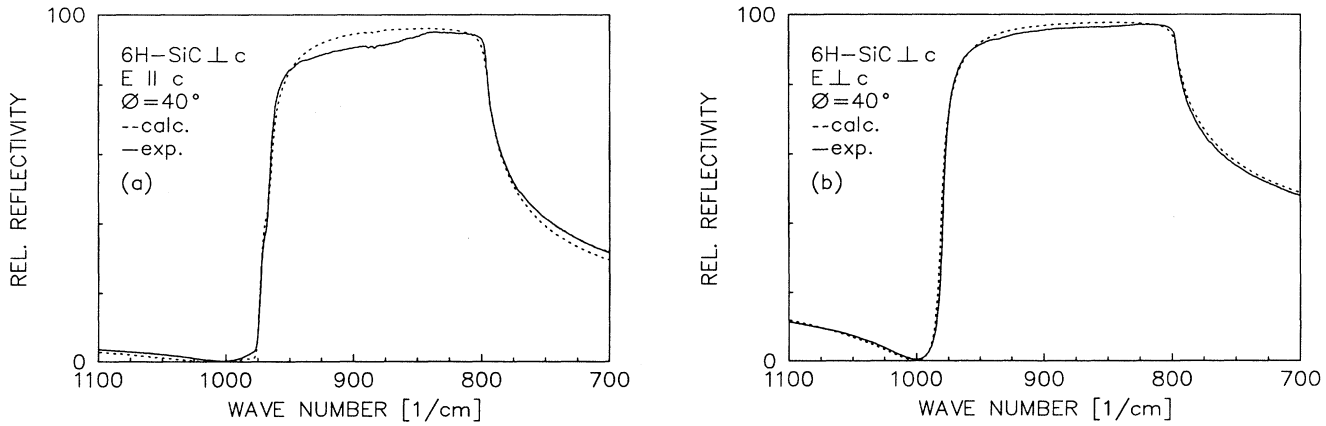

FIG. 4. (a) 6*H*-SiC reflectivity spectrum *G*1: ⊥ *c*-cut sample, $\mathbf{E}\|c,\phi=40°$; (b) 6*H*-SiC reflectivity spectrum *G*2: ⊥ *c*-cut sample, $\mathbf{E}\perp c,\phi=40°$; (c) 6*H*-SiC reflectivity spectrum *G*3: ∥ *c*-cut sample, $\mathbf{E}\|c,\phi=40°$. A new spike line appears at an angle of incidence of 40° in the extraordinary ray. (d) 6*H*-SiC reflectivity spectrum *G*4: ∥ *c*-cut sample, $\mathbf{E}\perp c,\phi=40°$.

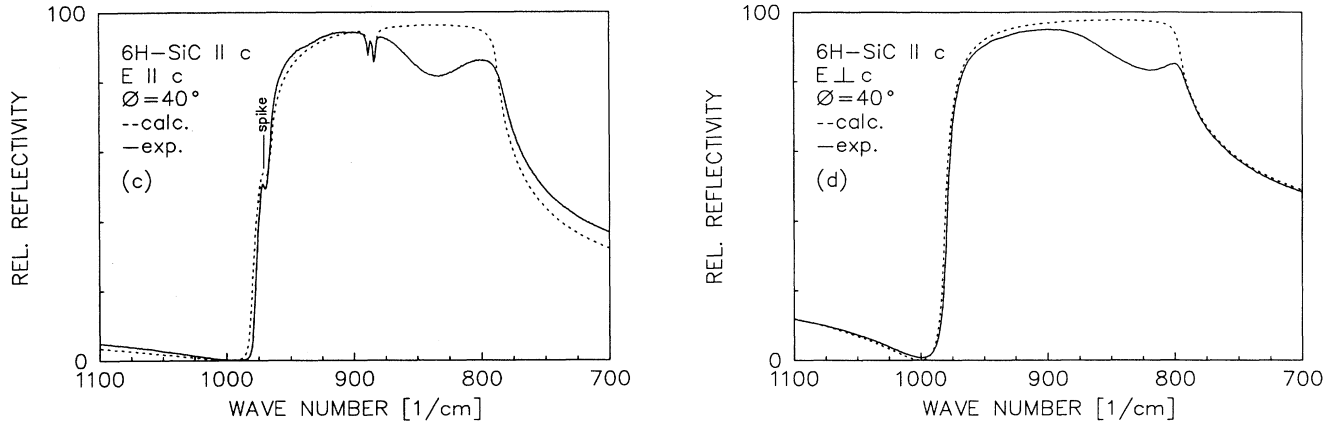

FIG. 4. (*Continued*).

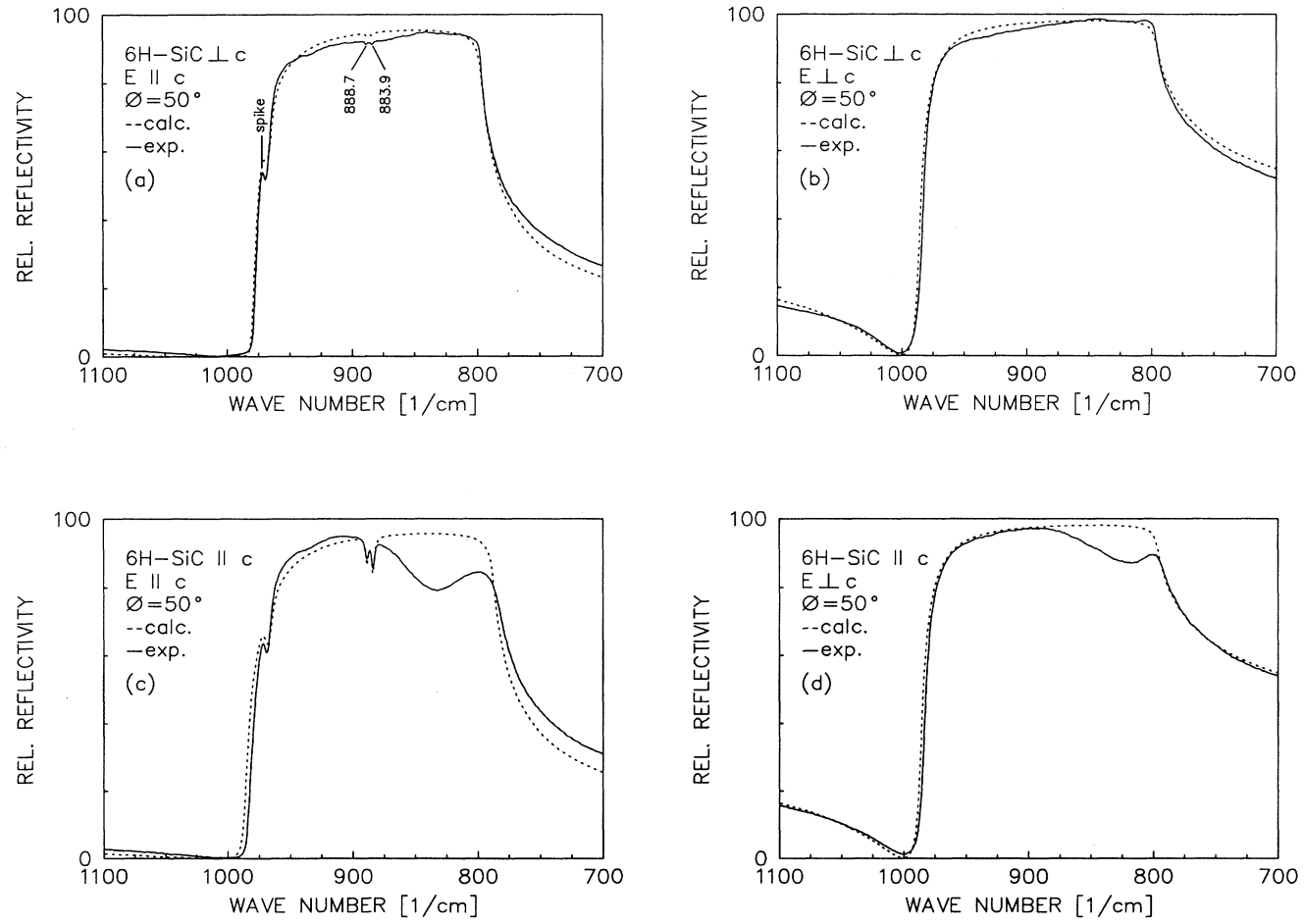

FIG. 5. (a) 6*H*-SiC reflectivity spectrum *G*1: ⊥ *c*-cut sample, $\mathbf{E}\|c, \phi = 50°$. The spike line appears also in geometry *G*1 at an angle of incidence of 50° in the extraordinary ray; also the two weak phonon lines in the middle of the reststrahl band are now observable here. (b) 6*H*-SiC reflectivity spectrum *G*2: ⊥ *c*-cut sample, $\mathbf{E}\perp c, \phi = 50°$; (c) 6*H*-SiC reflectivity spectrum *G*3: ∥ *c*-cut sample, $\mathbf{E}\|c, \phi = 50°$; (d) 6*H*-SiC reflectivity spectrum *G*4: ∥ *c*-cut sample, $\mathbf{E}\perp c, \phi = 50°$.

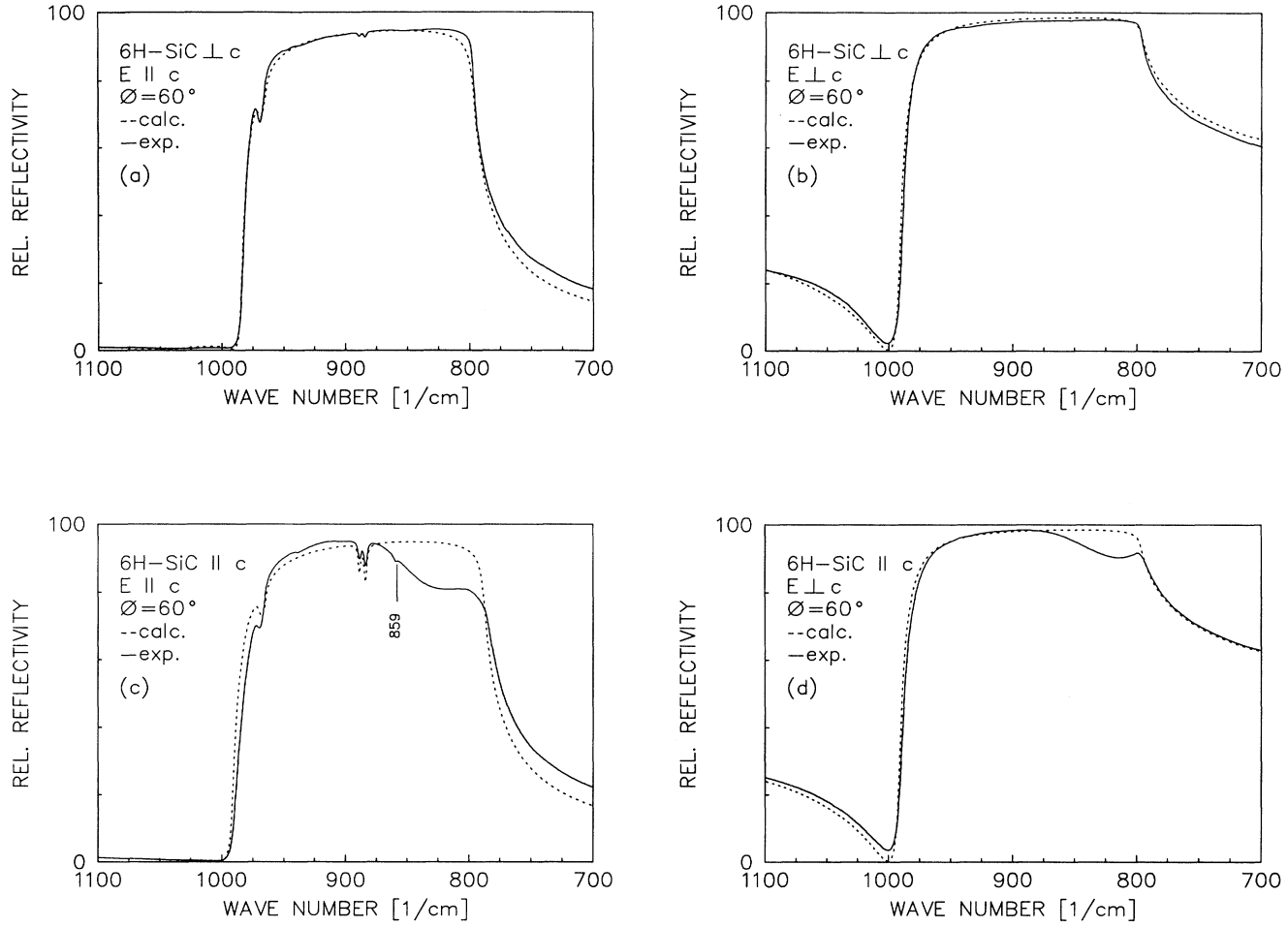

FIG. 6. (a) 6*H*-SiC reflectivity spectrum *G*1: ⊥ *c*-cut sample, $\mathbf{E}\|c, \phi = 60°$;(b) 6*H*-SiC reflectivity spectrum *G*2: ⊥ *c*-cut sample, $\mathbf{E}\perp c, \phi = 60°$; (c) 6*H*-SiC reflectivity spectrum *G*3: ∥ *c*-cut sample, $\mathbf{E}\|c, \phi = 60°$. The hump tends now to a more flat shape; a new structure at $\omega = 859\ \text{cm}^{-1}$ is visible. (d) 6*H*-SiC reflectivity spectrum *G*4: ∥ *c*-cut sample, $\mathbf{E}\perp c, \phi = 60°$.

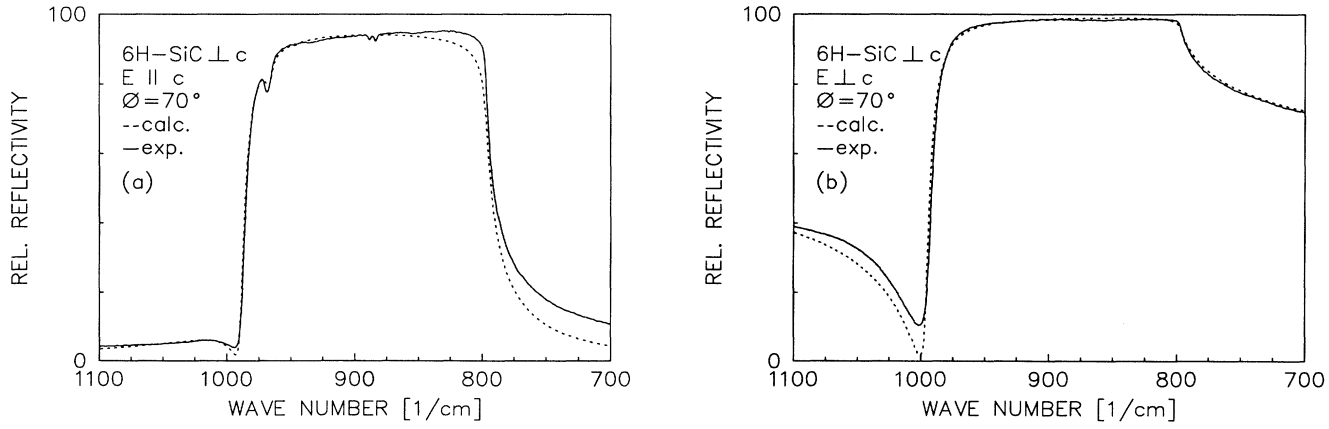

FIG. 7. (a) 6*H*-SiC reflectivity spectrum *G*1: ⊥ *c*-cut sample, $\mathbf{E}\|c, \phi = 70°$; (b) 6*H*-SiC reflectivity spectrum *G*2: ⊥ *c*-cut sample, $\mathbf{E}\perp c, \phi = 70°$; (c) 6*H*-SiC reflectivity spectrum *G*3: ∥ *c*-cut sample, $\mathbf{E}\|c, \phi = 70°$. The shape of the hump is totally deformed now; the structure at $859\ \text{cm}^{-1}$ has been increased. (d) 6*H*-SiC reflectivity spectrum *G*4: ∥ *c*-cut sample, $\mathbf{E}\perp c, \phi = 70°$.

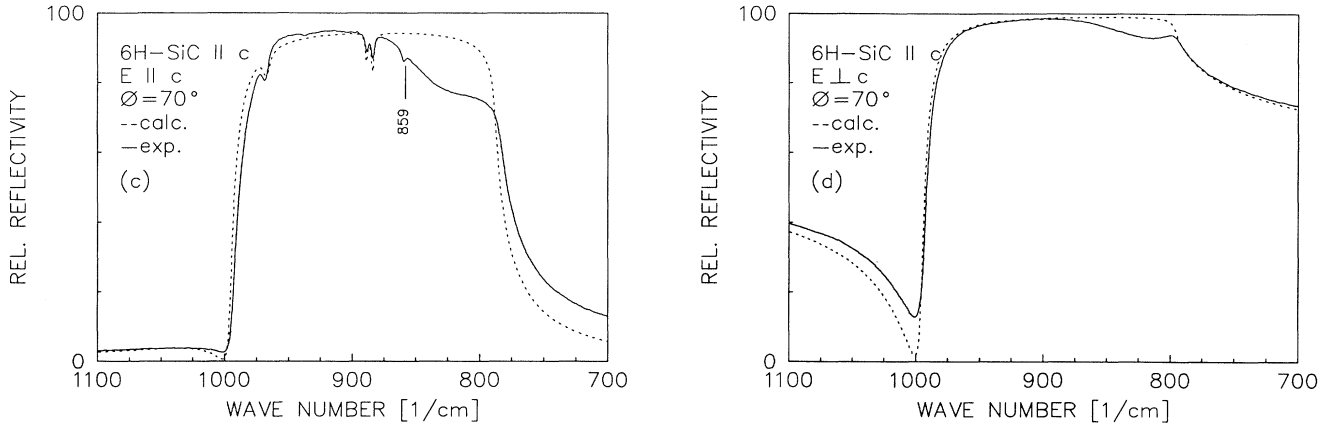

FIG. 7. (*Continued*).

the extraordinary ray at 60° angle of incidence [Fig. 6(c)] and was even more distinct at 70° [Fig. 7(c)]. It is remarkable that this line cannot be observed for small angles of incidence [Figs. 3(c) and 4(c)]. The origin of this line could not be identified.

(d) The appearance of this weak line at 859 cm^{-1} is correlated with the shape of the broad hump on the low energy side of the reststrahl band (at $\omega \approx 800$ cm^{-1}) in geometries $G3$ and $G4$. For $\mathbf{E} \| c$ in geometry $G3$ [Figs 3(c), 4(c), and 5(c)] its shape is nearly independent of the angle of incidence up to 50°, but at $\phi = 60°$ [Fig. 6(c)] it suddenly becomes flatter and at $\phi = 70°$ its shape decreases to longer wavelengths [Fig. 7(c)].

For $\mathbf{E} \perp c$ this hump is also observable in $\|c$-cut samples (geometry $G4$), although its shape here is less broad and nearly independent of the angle of incidence up to $\phi = 70°$ [Figs. 3(d), 4(d), 5(d), 6(d), and 7(d)].

The hump cannot be observed in samples cut perpendicular to the c axis independent of the angle of incidence and polarization ($G1$ [Figs. 3(a), 4(a), 5(a), 6(a), and 7(a)] and $G2$ [Figs. 3(b), 4(b), 5(b), 6(b), and 7(b)] geometries). This is remarkable when going to flatter angles of incidence, because the lines at 889 and 884 cm^{-1} in geometry $G3$ ($\mathbf{E} \|$ c in $\|$ c-cut samples) are observable—although weaker —in geometry $G1$ [$\mathbf{E} \| c$ in $\perp$ c-cut samples; cf. Fig. 5(a)]. The influence of crystal anisotropy on the shape of the described hump at $\omega \approx 800$ cm^{-1} should be very small. It is interesting to remark that Lauterbach [11] and Picus [3] have found an analogous humplike structure in the reststrahl band of a $\|$ c-cut 4H-SiC sample and another SiC sample (no specifications were given), respectively. Yet in the paper of Spitzer *et al.* on 6H-SiC (Ref. 4) this humplike structure did not appear. Such structures also have been found in other materials. We discuss here some arguments for their appearance, which are not connected with the surface properties of a sample, because such effects may be suppressed by the polishing procedure of the surface. For instance the reflectivity spectra of the alkali halogenides show distinct sidebands[39] which can be attributed to strong anharmonic effects in these materials leading to a frequency- and temperature-dependent damping $\Gamma = \Gamma(\omega, T)$.[40] Such a mechanism seems in principle possible for SiC, too, because of its relatively high polarity. However, this mechanism is excluded due to the strong crystal orientation dependence of the hump structure (visible in the $G3$ and $G4$ but not in the $G1$ and $G2$ geometries). A classical model of Barker and Hopfield[41] assumes that several energetically close resonances are coupling, leading to a reflectivity spectrum different from a spectrum of uncoupled resonances. In the case of 6H-SiC the oscillator strengths of the phonons at 777 and 769 cm^{-1} are much too small to explain such a strong effect. The fact that these weak phonons—in contrast to those in the reststrahl band—are not visible in the reflectivity spectrum is due to the high refractive index at their energy, while the lines at 889 and 884 cm^{-1} lie in a energy region of low refractive index (cf. Fig. 9). Spatial dispersion (cf. Sec. II) does not contradict the experimental results, but it should be negligible because of the former estimation. It is interesting that the reflectivity spectra of other semiconductor materials with a simpler crystal lattice than 6H-SiC also show structures of unknown origin in the reststrahl band.[42]

V. NUMERICAL RESULTS

As a consequence of the directional dispersion in 6H-SiC, an exact calculation of reflectivity is possible only for the ordinary ray, because the dielectric function (5) here is independent upon the angle of incidence. In the case of the extraordinary ray the dielectric function (5) depends on the angle θ between the c axis and the direction of wave propagation and therefore on the angle of incidence due to the refraction law (except in the case of normal incidence). This problem can be solved only by a self-consistent calculation. Our calculations were not self-consistent. Spatial dispersion due to the phonon dispersion relation was also not taken into account.

The starting points for the calculation of the functions $\epsilon_\perp$ and $\epsilon_\|$ were the anisotropic dispersion formulas (5). The phonon energies were taken from the Raman-

TABLE I. IR active phonons in 6*H*-SiC: $\mathbf{E}\perp c$.

Energy (cm^{-1})	Symmetry	$x=q/q_{max}$	Strength
797	E_1	0	Strong
777	E_1	0.67	Weak
769	E_1	0.67	Weak
241	E_1	0.67	Weak
236	E_1	0.67	Weak

TABLE II. IR active phonons in 6*H*-SiC: $\mathbf{E}\parallel c$.

Energy (cm^{-1})	Symmetry	$x=q/q_{max}$	Strength
888.7	A_1	0.67	Weak
883.9	A_1	0.67	Weak
788	A_1	0	Strong
508	A_1	0.67	Weak
504	A_1	0.67	Weak

scattering measurements of Feldman *et al.*[37] (cf. Tables I and II; the phonons 241 and 236 cm^{-1} were not included into the following calculations, because the necessary experimental data were not available). For evaluation of the above parameters ϵ_∞, ρ_i, ω_i, and Γ_i first the parameters of the strongest phonon ω_{TO} and then the parameters of the residual (much weaker) phonons were determined. The experimental base for the determination of these parameters was the phonon energies ω_{TO}, ω_{LO} and the minima of the reflectivity spectra, ω_m, for the ordinary and extraordinary rays, respectively. $\omega_{TO}^{\perp}$, $\omega_{TO}^{\parallel}$, $\omega_{LO}^{\perp}$, $\omega_{LO}^{\parallel}$ are shown in Table III, while $\omega_m^{\perp}=1000.0\pm0.5$ cm^{-1} and $\omega_m^{\parallel}=992.7\pm0.5$ cm^{-1} were taken from our measurements at $\phi=30°$. For low angles of incidence ϕ, the dependence of $\omega_m^{\perp}$ and $\omega_m^{\parallel}$ on ϕ is supposed to be negligible. From $R(\omega_m)\approx 0$ one can derive the equation

$$\epsilon_1(\omega_m)\approx 1\approx\epsilon_\infty+\frac{4\pi\rho(\omega_0^2-\omega_m^2)}{(\omega_0^2-\omega_m^2)^2+\Gamma^2\omega_m^2} . \tag{9}$$

Together with the GLST relation Eq. (2),

$$\frac{\epsilon_0}{\epsilon_\infty}=\frac{\omega_{LO}^2+\frac{1}{4}\Gamma^2}{\omega_{TO}^2+\frac{1}{4}\Gamma^2} , \tag{10}$$

and the equation

$$\epsilon_0=\epsilon_\infty+4\pi\rho , \tag{11}$$

Eq. (9) was used to calculate the unknown quantities ϵ_0, ϵ_∞, and ρ, which only weakly depend upon the parameter Γ. Γ was assumed to be an isotropic constant and determined by fitting the reflectivity spectrum of a sample with very good surface quality (cf. Ref. 43) which yielded $\Gamma=0.0068$. From these values we obtained $\epsilon_\infty^{\perp}=6.17$ and $\epsilon_\infty^{\parallel}=6.49$. With the known parameters of the two strong phonons, it was easy to determine the parameters for the weak phonons. For that reason the corresponding peaks in the reflectivity and transmission spectra were fitted (e.g., Fig. 8). It was not possible to fit the phonon structures at 777 cm^{-1} and 769 cm^{-1} because they could not be observed in the reflectivity spectrum, due to the high refractive index in this region. It also was difficult to observe these in transmission measurements, because of the overlapping high absorption of the strong phonon ω_{TO}.

The phonon oscillator parameters in 6*H*-SiC determined by this method are shown in Table III.

The directional dispersion of the strong phonons ω_{LO} and ω_{TO} (cf. Ref. 37) was taken into account as follows. For non-normal incidence of radiation the striking wave of the extraordinary ray is refracted by a determined angle towards the c axis (cf. Ref. 24). For $\omega\approx\omega_{TO}$ the refractive index n is much higher than 1, and so the ray is refracted almost perpendicular to the surface. However, for $\omega\approx\omega_{LO}$, n is much smaller than 1 and the refracted ray is nearly parallel to the surface. Due to the strongly varying refractive index in the infrared—different from the visible spectral region where the Raman experiments were performed ($n\approx 2.7=$const)—the phonon pairs (ω_{LO}, ω_{TO}) (970 cm^{-1}, 797 cm^{-1}) for $\mathbf{E}\perp c$ and (964 cm^{-1}, 788 cm^{-1}) for $\mathbf{E}\parallel c$ belong together. We checked this argument carrying out the above calculations with the unchanged Raman values and obtained $\rho_\perp=0.190$, $\rho_\parallel=0.335$, $\epsilon_\infty^{\perp}=5.16$, and $\epsilon_\infty^{\parallel}=8.18$. These values also give a good description of the reflectivity spectrum in the reststrahl region, but a much too high optical anisotropy in the infrared area below 700 cm^{-1} and above 1200 cm^{-1}. For the calculation of reflectivity the Fresnel formulas[44] were adjusted to the different experimental geometries as follows. $G1{:}\perp$ c-cut sample; $\mathbf{E}\parallel c$,

TABLE III. Parameters of the lattice oscillators in 6*H*-SiC.

Energy (cm^{-1})		ρ_i	Γ_i	Symmetry	$x=q/q_{max}$	Strength
970	LO $\perp$			E_1	0	Strong
964	LO $\parallel$			A_1	0	Strong
888.7		9.46×10^{-5}	2.41×10^{-3}	A_1	0.67	Weak
883.9		1.86×10^{-4}	3.11×10^{-3}	A_1	0.67	Weak
797	TO $\perp$	0.236	6.8×10^{-3}	E_1	0	Strong
788	TO $\parallel$	0.257	6.8×10^{-3}	A_1	0	Strong
777		Not determined	Not determined	E_1	0.67	Weak
769		Not determined	Not determined	E_1	0.67	Weak
508		4.0×10^{-6}	1.5×10^{-3}	A_1	0.67	Weak
504		1.7×10^{-5}	2×10^{-3}	A_1	0.67	Weak

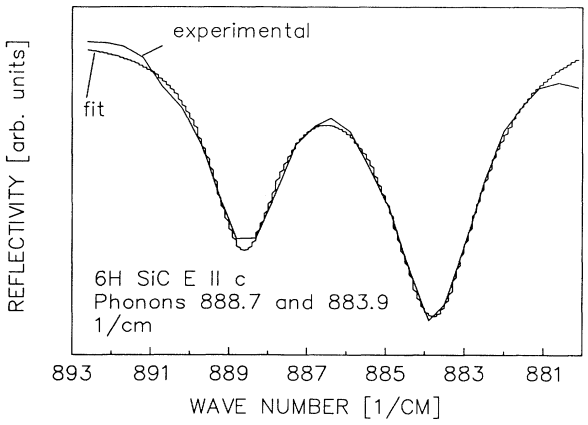

FIG. 8. Fit of the weak phonons 889 cm^{-1} and 883 cm^{-1} in 6*H*-SiC in the reststrahl region for $\mathbf{E}\|c$.

$$R_{\|}=|r_{\|}|^2\ ,\quad r_{\|}=\frac{\sqrt{\epsilon^{\perp}\epsilon^{\|}}\cos(\phi)-\sqrt{\epsilon^{\|}-\sin(\phi)^2}}{\sqrt{\epsilon^{\perp}\epsilon^{\|}}\cos(\phi)+\sqrt{\epsilon^{\|}-\sin(\phi)^2}}\ ; \tag{12}$$

*G*2: $\perp$ *c*-cut sample, $\mathbf{E}\perp c$,

$$R_{\perp}=|r_{\perp}|^2\ ,\quad r_{\perp}=\frac{\cos(\phi)-\sqrt{\epsilon^{\perp}-\sin(\phi)^2}}{\cos(\phi)+\sqrt{\epsilon^{\perp}-\sin(\phi)^2}}\ ; \tag{13}$$

*G*3: $\|$ *c*-cut sample, $\mathbf{E}\|c$,

$$R_{\|}=|r_{\|}|^2\ ,\quad r_{\|}=\frac{\sqrt{\epsilon^{\|}\epsilon^{\perp}}\cos(\phi)-\sqrt{\epsilon^{\perp}-\sin(\phi)^2}}{\sqrt{\epsilon^{\|}\epsilon^{\perp}}\cos(\phi)+\sqrt{\epsilon^{\perp}-\sin(\phi)^2}}\ ; \tag{14}$$

*G*4: $\|$ *c*-cut sample, $\mathbf{E}\perp c$,

$$R_{\perp}=|\mathbf{r}_{\perp}|^2\ ,\quad r_{\perp}=\frac{\cos(\phi)-\sqrt{\epsilon^{\perp}-\sin(\phi)^2}}{\cos(\phi)+\sqrt{\epsilon^{\perp}-\sin(\phi)^2}}\ . \tag{15}$$

These anisotropic reflectivity formulas show that within the approximations used here, there is no difference between the geometries *G*2 ($\perp$ *c* sample, $\mathbf{E}\perp c$) and *G*4 ($\|$ *c* sample, $\mathbf{E}\perp c$) in contrast to the experiment. For numerical calculations the above equations were used in real form which can be found in Refs. 45 and 46. With the oscillator parameters from Table III we obtained the theoretical reflectivity spectra in good agreement with the experiments [cf. Figs. 3–7]. The spike curve, which is due to crystal anisotropy (cf. Sec. II), was in very good agreement with the measurements (angle and polarization dependence). The optical constants *n* and *k* for $\mathbf{E}\perp c$ and $\mathbf{E}\|c$ are shown in Figs. 9 and 10. It is interesting to note that the sharp peaks at 888.7 cm^{-1} and 883.9 cm^{-1} are observable due to a high relative change in the refractive index and not by an increase of the absorption coefficient. Their calculated angle and polarization dependence describes the measurements very well. The broad hump in the spectra (780 $cm^{-1} \le \omega \le 880\ cm^{-1}$) of the $\|$ *c*-cut samples did not appear in the result of the numerical calculations. As we expected it obviously cannot be described with the simple Lorentz oscillator model. So one can exclude crystal anisotropy as the reason for it. The origin of the broad hump remains unknown. Furthermore we calculated the transmission spectra of a 700 μm thick sample with the above parameters taking only one-phonon absorption processes into account (cf. Fig. 11).

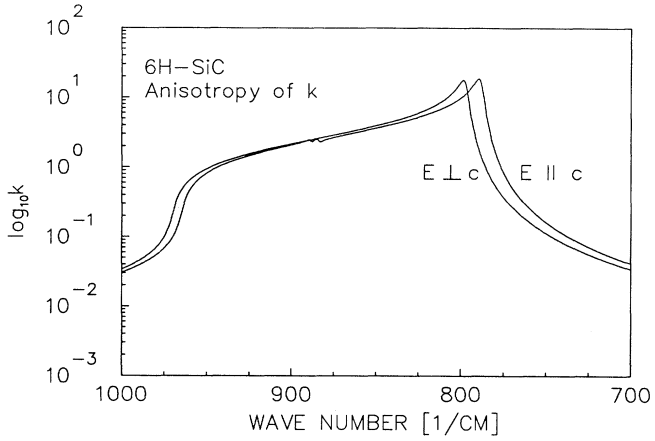

FIG. 10. Anisotropy of refraction index *k* for $\mathbf{E}\|c$ and $\mathbf{E}\perp c$: 1000–700 cm^{-1} (calculated, logarithmic scale).

VI. CONCLUSION

6*H*-SiC appears to be a good test crystal for interesting features in the reflection spectra of anisotropic crystals

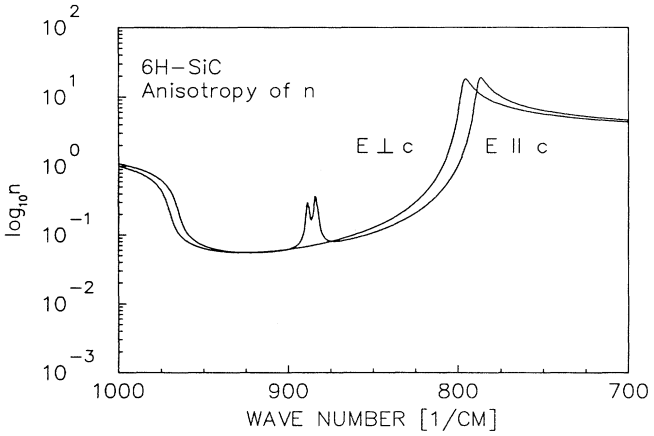

FIG. 9. Anisotropy of refraction index *n* for $\mathbf{E}\|c$ and $\mathbf{E}\perp c$: 1000–700 cm^{-1} (calculated, logarithmic scale).

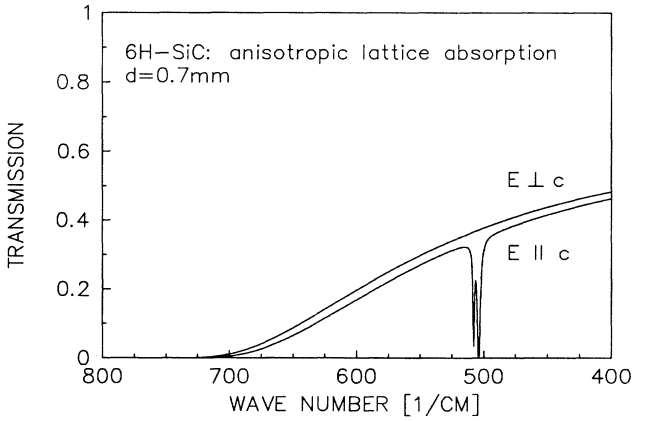

FIG. 11. Calculated transmission spectra for $\mathbf{E}\perp c$ and $\mathbf{E}\|c$ of a 700 μm thick 6*H*-SiC sample: 800–400 cm^{-1}.

when polarized radiation is used. This is due to the large number of infrared active phonons (ten IR active branches) in this material. We have presented an array of experimental reflectivity measurements of 6*H*-SiC which clearly demonstrate the influence of crystal anisotropy on the reststrahl band. We were able to show qualitatively and numerically that a spike curve in the extraordinary ray is due to crystal anisotropy. Also two weak phonon absorption lines in the reststrahl band of 6*H*-SiC could be well explained by the Lorentz oscillator model. It turned out that they are mainly visible due to a modulation of the refractive index n. A polarization-independent broad hump appeared in the spectra of the $\|$ c-cut samples. The origin of this structure is unknown.

Previous infrared reflectivity measurements of many anisotropic solids should be reinvestigated using different angles of incidence and polarized radiation. We also expect an observable effect of crystal anisotropy on reflectivity spectra due to interband transitions in these materials. Therefore the interpretation of these spectra must be done with great care when using the data for band-structure investigations.

ACKNOWLEDGMENTS

We are indebted to S. Leibenzeder and R. A. Stein of the Siemens Research Laboratories Erlangen for supplying the samples. We thank C. Haberstroh for determining the polytype by low temperature photoluminescence and A. Schöner for the Hall effect measurements.

[1]W. Coblentz, Carnegie Institution of Washington, Parts V, VI and VIII, 36 (1908).
[2]S. Schaefer and M. Thomas, Z. Phys. **12**, 330 (1923).
[3]G. Picus, in Z. Burstein and P. Egli, *Advances in Electronics and Electron Physics III,* edited by L. Marton (Academic, New York, 1955), Vol. 7, p. 1455.
[4]W. G. Spitzer, D. A. Kleinman, and D. Walsh, Phys. Rev. **113**, 127 (1959).
[5]W. G. Spitzer, D. A. Kleinman, and C. Frosch, Phys. Rev. **113**, 133 (1959).
[6]M. A. Il'in and E. P. Rashevskaya, Fiz. Tekh. Poluprovodn. **5**, 1658 (1971) [Sov. Phys. Semicond. **5**, 1454 (1972)].
[7]M. A. Il'in, A. A. Kukharskii, E. P. Rashevskaya, and V. K. Subashiev, Fiz. Teverd. Tela (Leningrad) **13**, 2478 (1971) [Sov. Phys. Solid State **13**, 2078 (1972)].
[8]I. M. Purtseladze and L. G. Khavtasi, Fiz. Tekh. Poluprovodn. **5**, 1871 (1971) [Sov. Phys. Semicond. **5**, 1628 (1972)].
[9]M. A. Il'in and E. P. Rashevskaya, Fiz. Tekh. Poluprovodn. **6**, 1404 (1972) [Sov. Phys. Semicond. **6**, 1228 (1973)].
[10]R. T. Holm, P. H. Klein, and P. E. R. Nordqiust, Jr., J. Appl. Phys. **60**, 1479 (1986).
[11]T. Lauterbach, diploma thesis, University of Erlangen-Nürnberg, 1988.
[12]R. Helbig, Phys. Scr. T **35**, 194 (1991).
[13]M. F. MacMillan, W. J. Choyke, and R. P. Devaty, in *Amorphous and Crystalline Silicon Carbide IV,* edited by C. Y. Yang, M. M. Rahman, and G. L. Harris, Springer Proceedings in Physics Vol. 71 (Springer-Verlag, Berlin, 1992).
[14]F. Engelbrecht, diploma thesis, University of Erlangen–Nürnberg, 1992.
[15]M. Balkanski, in *Handbook on Semiconductors,* edited by T. S. Moss (North-Holland, Amsterdam, 1980), Vol. 2.
[16]M. Born and K. Huang, *Dynamical Theory of Crystal Lattices* (Clarendon, Oxford, 1954).
[17]B. Donovan and J. F. Angress, *Lattice Vibrations* (Chapman and Hall, London, 1971).
[18]F. Wooten, *Optical Properties of Solids* (Academic, New York, 1972).
[19]R. F. Wallis and A. A. Maradudin, Phys. Rev. **125**, 1277 (1962).
[20]R. F. Wallis and M. Balkanski, *Many-Body Aspects of Solid State Spectroscopy* (North-Holland, Amsterdam, 1986).
[21]I. F. Chang, S. S. Mitra, J. N. Plendl, and L. C. Mansur, Phys. Status Solidi B **28**, 663 (1968).
[22]R. H. Lyddane, R. G. Sachs, and E. Teller, Phys. Rev. **59**, 673 (1941).
[23]V. M. Agranovich and V. L. Ginzburg, *Crystal Optics with Spatial Dispersion, and Excitons* (Springer-Verlag, Berlin, 1984).
[24]L. D. Landau and E. M. Lifschitz, *Electrodynamics of Continuous Media,* Course of Theoretical Physics Vol. 8 (Pergamon, New York, 1960).
[25]R. Loudon, Adv. Phys. **13**, 423 (1964).
[26]R. Claus, Phys. Status Solidi B **50**, 11 (1972).
[27]R. Claus, Phys. Status Solidi B **100**, 9 (1980).
[28]J. J. Hopfield and D. G. Thomas, Phys. Rev. **132**, 563 (1963).
[29]K. Hümmer, Exzitonische Polaritonen in einachsigen Kristallen (Habitilation, Erlangen, 1978).
[30]I. G. Lang and U. S. Pashabekova, Fiz. Tverd. Tela (Leningrad) **6**, 3640 (1965) [Sov. Phys. Solid State **6**, 2913 (1965)].
[31]G. Ziegler, P. Lanig, D. Theis, and C. Weyrich, IEEE Trans. Electron Devices **ED-30**, 277 (1983).
[32]L. Merten, Z. Naturforsch. Teil A **23**, 1183 (1968).
[33]L. Merten and G. Lamprecht, Phys. Status Solidi **39**, 573 (1970).
[34]G. Lamprecht and L. Merten, Phys. Status Solidi **55**, 33 (1973).
[35]W. J. Choyke, in *The Physics and Chemistry of Carbides, Nitrides and Borides,* NATO ASI Series Vol. 185 (Kluwer, Dordrecht, 1990), p. 563.
[36]A. T. Collins, E. C. Lightowlers, and P. J. Dean, Phys. Rev. **158**, 833 (1967).
[37]D. W. Feldman, James H. Parker, Jr., W. J. Choyke, and Lyle Patrick, Phys. Rev. **170**, 698 (1968).
[38]P. M. A. Sherwood, *Vibrational Spectroscopy of Solids* (Cambridge University Press, Cambridge, England, 1972).
[39]L. Genzel, Festkörperprobleme **6**, 32 (1967).
[40]H. Bilz, Vibrational Infrared and Raman Spectra of Non-Metals, in S. Flügge, Handbuch der Physik Band XXV/2d, Licht and Materie Id (Springer-Verlag, Berlin, 1984).
[41]A. J. Barker, Jr. and J. J. Hopfield, Phys. Rev. **135**, A1732 (1964).
[42]M. Hass and B. W. Henvis, J. Phys. Chem. Solids **23**, 1099 (1962).
[43]S. Karmann, W. Suttrop, A. Schöner, M. Schadt, C. Haberstroh, F. Engelbrecht, R. Helbig, G. Pensl, R. A. Stein, and S. Leibenzeder, J. Appl. Phys. **72**, 5437 (1992).
[44]P. Brüesch, *Phonons: Theory and Experiments II* (Springer-Verlag, Berlin, 1986), Appendix B.2.
[45]D. L. Greenaway, G. Harbeke, F. Bassani, and E. Tosatti, Phys. Rev. **178**, 1340 (1968).
[46]L. P. Mosteller, Jr. and F. Wooten, J. Opt. Soc. Am. **58**, 511 (1968).